Champlane Deep Galactic Bulge Survey. I. Faint Accretion-driven Binaries in the Limiting Window

Citation

Permanent link

Terms of Use

Share Your Story

Accessibility

CHAMPLANE DEEP GALACTIC BULGE SURVEY. I. FAINT ACCRETION-DRIVEN BINARIES IN THE LIMITING WINDOW

Maureen van den Berg[1], JaeSub Hong[1], Jonathan E. Grindlay[1]

Draft version November 9, 2018

ABSTRACT

We have carried out a deep X-ray and optical survey with *Chandra* and *HST* of low-extinction regions in the Galactic bulge. Here we present the results of a search for low-luminosity ($L_X \lesssim 10^{34}$ ergs s^{-1}) accreting binaries among the *Chandra* sources in the region closest to the Galactic Center, at an angular offset of 1.4°, that we have named the Limiting Window. Based on their blue optical colors, excess Hα fluxes, and high X-ray–to–optical flux ratios, we identify three likely accreting binaries; these are probably white dwarfs accreting from low-mass companions (cataclysmic variables or CVs) although we cannot exclude that they are quiescent neutron-star or black-hole low-mass X-ray binaries. Distance estimates put these systems farther than $\gtrsim 2$ kpc. Based on their Hα-excess fluxes and/or high X-ray–to–optical flux ratios, we find 22 candidate accreting binaries; however, the properties of some can also be explained if they are dMe stars or active galaxies. We investigate the CV number density towards the bulge and find that the number of observed candidate CVs is consistent with or lower than the number expected for a constant CV-to-star ratio that is fixed to the local value. Our conclusions are limited by uncertainties in the extinction (for which we see a ~30% variation in our 6.6′×6.6′ field) and selection effects. The X-ray properties of two likely CVs are similar to those of the faint, hard X-ray sources in the Galactic-Center region that have been explained by (mainly) magnetic CVs. If our candidates belong to the same population, they would be the first members to be optically identified; optical or infrared identification of their Galactic-Center analogs would be impossible due to the higher obscuration. We speculate that all Galactic hard X-ray sources in our field can be explained by magnetic CVs.

Subject headings: X-rays: binaries — novae, cataclysmic variables — Galaxy: bulge — surveys

1. INTRODUCTION

With its sharp view, the *Chandra* X-ray Observatory has revealed a large population of X-ray point sources along the line of sight towards the central 40 pc of our Galaxy (Muno et al. 2003). The majority of these are faint ($L_X \approx 10^{31-34}$ ergs s^{-1}) and have intrinsically hard X-ray spectra. Comparison with the X-ray properties of candidate local analogs suggests that the Galactic-Center sources are a mix of compact objects (white dwarfs, neutron stars and black holes) accreting from binary companions. From the small fraction of sources with bright ($K < 15$) infrared candidate counterparts, Laycock et al. (2005) excluded that the contribution of neutron stars in wind-fed Be high-mass X-ray binaries (HMXBs) exceeds ~10%; on the other hand, a significant contribution from wind-fed HMXBs to X-ray sources in the central $2° \times 0.8°$ had been suggested by Pfahl et al. (2002). This leaves magnetic white dwarfs accreting from low-mass companions (i.e. magnetic cataclysmic variables or CVs) as the most likely dominating source class, as had been suggested by Muno et al. (2004). However, this also leaves us with the enormous challenge to identify these sources at other wavelengths: CVs in the Galactic Center are too faint to be detected in the infrared (unless they undergo a nova or bright dwarf-nova outburst), and the Galactic-Center region is too heavily obscured by dust to search for counterparts in the optical. At the same time, by the sheer number of Galactic-Center X-ray sources (thousands), this population has great importance for understanding the Galactic accreting binary content and unraveling the evolutionary history of the inner Galaxy.

As part of the *Chandra* Multi-wavelength Plane survey (*ChaMPlane*; Grindlay et al. 2005), we have carried out an

X-ray and optical survey of deep, near-simultaneous *Chandra* and *HST* pointings of three low-extinction regions, or *Windows*, in the Galactic bulge. These Windows lie on a nearly radial alignment with the Galactic Center, at angular offsets between 1.4° and 4°. One of the aims of this survey is to look for signatures of a population of faint, hard X-ray sources similar to the one found by Muno et al. (2003), and take advantage of the more favorable conditions for source identification compared to the Galactic Center. Indeed, based on the spatial distribution of *Chandra* sources in these three and four more inner-bulge fields, Hong et al. (2009) (H09) show that this population can be traced out to at least 1.4° from the Galactic Center, i.e. out to our "innermost" Window. We have named this field the Limiting Window (LW) because extinction rapidly increases (and therefore chances for optical identification drastically decline) when moving closer to the Galactic Center. In this paper we try to identify X-ray binaries (that will be most likely CVs given their relative abundance) among *Chandra* sources in the LW by searching for optical counterparts; by extrapolation, this could also shed light on the nature of the Galactic-Center sources.

Another main goal of our Windows survey is to study for the first time the population of CVs towards the bulge. Much of what we know about the Galactic CV population is based on a sample of relatively local systems, mainly within ~2 kpc from the Sun (see, for example, Warner (1995), Ak et al. (2008)). Our deep *Chandra* exposures have the sensitivity to detect bright ($L_X \gtrsim 10^{31}$ ergs s^{-1}) CVs at $\gtrsim 8$ kpc, which means we can significantly increase the depth of existing CV samples. In a follow-up paper we will combine our results for the LW with the search for CVs and other accreting binaries in our other two Windows—Baade's and Stanek's Windows (initial results were already given in van den Berg et al. (2006)). Limits on the CV space density towards the Galac-

[1] Harvard-Smithsonian Center for Astrophysics, 60 Garden Street, Cambridge, MA 02138, USA; maureen@head.cfa.harvard.edu

tic anti-Center were derived by Grindlay et al. (2005) from *ChaMPlane* data.

After describing the X-ray and optical observations in §2, we outline the analysis steps in §3. We present the identified candidate CVs in §4, and discuss our results in the contexts of the Galactic CV population and the Galactic-Center X-ray–source population in §5. We end with our conclusions in §6.

2. OBSERVATIONS

2.1. *Chandra data*

The Limiting Window was observed for 100 ks with the *Chandra*/ACIS-I aimpoint placed at Galactic coordinates $(l,b)=(0.10°,-1.43°)$. Due to observatory constraints, the observation was split in three exposures: ObsID 6362 (2005 Aug 19, 38 ks), ObsID 5934 (2005 Aug 22, 41 ks) and ObsID 6365 (2005 Oct 25, 21 ks). We stacked the three images into a single image; in the remainder of the paper we only consider the stacked pointing. The data were processed with the *ChaMPlane* X-ray data-reduction pipeline (Hong et al. 2005). We performed source detection on images in a soft (0.3–2.5 keV), hard (2.5–8 keV) and broad (B_x = 0.3–8 keV) energy band, and merged the resulting source lists into a master catalog following the procedures described in H09. A total of 319 ACIS-I sources are detected. The pipeline products that we mainly use in this paper are source positions and corresponding 95% confidence radii r_{95}, net source counts in the B_x band extracted from a region enclosing 95% of the energy at 1.5 keV, and energy quantiles E_x denoting the energies below which x% of the counts in the B_x band are detected. We use the latter to constrain X-ray spectral parameters for low-count sources; see Hong et al. (2004) for a description of the quantile method. The complete *Chandra* source list can be found in H09.

2.2. *HST/ACS data*

We observed with *HST* the inner area of the ACIS field with a 2×2 mosaic of slightly overlapping pointings of the Wide Field Camera (WFC) on the Advanced Camera for Surveys (ACS). The observations (program GO-10353) were carried out simultaneous with the first *Chandra* exposure (2005 Aug 19). A single WFC pointing images a 3.4′×3.4′ field with ~0.05″ pixels using two CCD detectors separated by a 2.5″ gap. Exposures were taken through the F435W ("B_{435}"), F625W ("R_{625}", similar to Sloan r) and F658N (Hα) filters. Each tile of the mosaic was observed with the same exposure sequence: 4×492 s in F435W, 168 s + 2×167 s in F625W and 4×496 s + 4×492 s in F658N. The offsets in Galactic coordinates $(\Delta l, \Delta b)$ of each *HST* pointing from the center of the *Chandra* pointing are (−0.04°,+0.01°), (+0.04°,−0.01°), (+0.01°,+0.04°) and (−0.01°,−0.04°). No dithering was applied to fill in the WFC chip gap. After boresight correction (see §3.5), 100 *Chandra* sources are included in the field of view of the ACS mosaic, including one source whose 95% X-ray error circle lies partially in the chip gap. The sources that are covered by our ACS mosaic are listed in Table 1.

3. ANALYSIS

3.1. *ACS photometry*

Photometry is performed using the stellar-photometry package DOLPHOT[2], a modified version of the HSTphot package

[2] http://purcell.as.arizona.edu/dolphot

to do photometry on *HST*/WFPC2 images (Dolphin 2000). DOLPHOT is equipped with a module for doing photometry on ACS images which uses a look-up table to help determine the spatially varying point spread function (PSF) at each detector location. We run DOLPHOT on the B_{435}, R_{625} and Hα images separately. The filter-dependent model PSFs are used as initial guesses for the actual PSFs of the images being analyzed; the former are slightly adjusted using isolated stars to correct for observation-specific focus and/or thermal conditions of the telescope. For stars with a signal-to-noise ratio (S/N) lower than 10 aperture photometry is used. Source detection is run twice, with sources that are detected in the first pass removed during the second pass. Then, for each star, a photometric solution is iteratively derived with the sky and neighbors subtracted until the photometry of the star and its neighbors converge to a stable solution. Sources that are separated by fewer than 2 pixels are merged into a single source.

DOLPHOT runs on the distorted (`flt`) images to avoid photometry errors associated with the pixel resampling that is necessary to correct for the significant geometric distortion of ACS images. The resulting output catalog, however, is aligned to a distortion-corrected (`drz`) image constructed with the STScI task *multidrizzle*. Optical source catalogs are derived for each filter separately; these are combined using a match criterion of a maximum separation of 1.5 pixels. DOLPHOT produces magnitudes for a 4-pixel aperture that are corrected for charge-transfer efficiency degradation. We compute a filter-dependent aperture correction to 10 pixels using aperture photometry of a few isolated stars; these corrections are between −0.08 and −0.10 mag. Together with the aperture corrections from 10 pixels to "infinity" and the zero-point offsets (Sirianni et al. 2005) they are applied to obtain calibrated photometry in the STMAG system. The approximate detection limits for $S/N = 5$ are $B_{435} \approx 27$, $R_{625} \approx 26.7$, and Hα ≈ 25.6.

In an attempt to remove artifacts and non-stellar objects from the source list, we generally only consider stars with $\chi^2 \leq 3$, $S/N \geq 5$, $-0.5 \leq$ sharpness $\leq +0.5$, crowding ≤ 2 mag, error flags < 8 and object classifications appropriate for stellar sources (type ≤ 2) in all three filters; see the DOLPHOT manual for details. Even after applying these criteria, the final source list is not guaranteed to be free of artifacts. For example, in the R_{625} versus $B_{435} - R_{625}$ color-magnitude diagrams (CMDs) a small number ($\lesssim 2\%$ of the total number of sources detected in all three bands) of faint, blue sources ($R_{625} > 22.5$, $B_{435} - R_{625} < 2$) is prominent. Upon closer inspection, most turn out to be associated with PSF artifacts near bright stars. For the CMDs and color-color

diagrams (CCDs) in this paper we have manually cleaned this region of the CMD from artifacts, which explains the sharp "boundaries" around this region in Figs. 2 and 4 (left). For the identification of candidate counterparts to *Chandra* sources, however, we visually inspect *all* detections in the search area (§3.5) to check that no valid optical source is erroneously eliminated and that no artifact is mistaken for a real source.

We run DOLPHOT in the artificial-star mode to estimate the detection completeness. For each of the magnitudes $R_{625}=18$, 19, ..., 25 we create catalogs with 9000–9500 fake stars; B_{435} and Hα magnitudes are assigned according to the mean $B_{435} - R_{625}$ and H$\alpha - R_{625}$ colors for that bin. The photometry is repeated in each filter after adding each fake star in turn to the image. We then check if the fake star is retrieved within 1 pixel of the input position and 0.2 mag of the input magnitude. These tests were done for one chip (1/8 of the field of view) only. We find that the completeness is ≥93% for $R_{625} = 22$ and drops to ~27% for $R_{625} = 25$.

3.2. *Improvement of the HST absolute astrometry*

The coordinates in the optical catalogs are corrected for geometric distortion but the *HST* absolute astrometry can be off by up to 3″ (see Koekemoer et al. 2005). To improve the astrometric accuracy, we tie the optical astrometry to the International Celestial Reference System (ICRS) using stars in the UCAC2 catalog that have a positional accuracy better than 0.070″ (Zacharias et al. 2004). Since UCAC2 stars are scarce and often saturated in the ACS images, we use a ground-based *V*-band image of the LW to derive secondary astrometric standards as an intermediate step. The ground-based image was obtained with the CTIO-4m Mosaic camera (field of view 36′×36′) and reduced following the procedures described in Zhao et al. (2005).

We first derive an astrometric solution for a section of the CTIO Mosaic image that includes the full ACS mosaic using 132 UCAC2 stars. Fitting for zero point, rotation angle, scale factor and distortions results in a solution with rms residuals of 0.040″ in right ascension and 0.036″ in declination. Next, the solution is transferred to one distortion-corrected image of each ACS pointing using sets of ~200 secondary standards selected from stars that are unsaturated and relatively isolated in the Mosaic and ACS images; we choose the stacked F658N images for this purpose which should be clean of cosmic rays and other artifacts given the large number of individual exposures. The resulting fits for zero point, rotation angle and scale factor have rms residuals of, typically, 0.02″ in each coordinate. Finally, the solutions are transferred to all ACS images of a given pointing using ~2000 tertiary standards; the associated errors are negligible. We estimate the final 1σ accuracy with which the optical astrometry is tied to the ICRS (σ_o) as the quadratic sum of the errors in the UCAC2 astrometry, the UCAC2–Mosaic tie and the Mosaic–*HST* tie, i.e. 0.090″– 0.095″. We adopt a uniform value of 0.095″ for all pointings.

3.3. *Extinction*

Extinction along the line of sight towards the LW is relatively low for a bulge field but not entirely negligible, and needs to be considered in order to derive intrinsic (unabsorbed) X-ray and optical fluxes. In Fig. 1 we compare two estimates from the literature of the extinction as function of distance. The three-dimensional A_V maps by Drimmel et al. (2003) (D03) are based on a model for the Galactic dust distribution but are rescaled to match COBE far-infrared data; the maps are thus limited to a resolution of ~0.35°×0.35°.
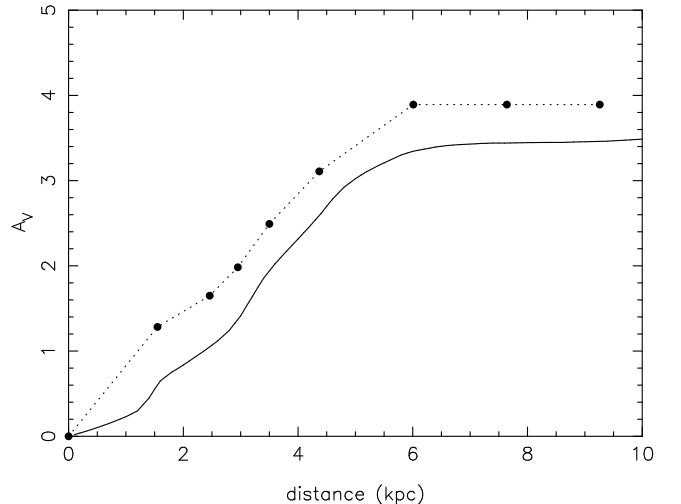

Fig. 1.— Extinction A_V towards the LW as function of distance as predicted by D03 (solid line) and M06 (dotted line). For the latter, we have assumed $A_V = 8.3 \times A_{Ks}$. In our analysis, we adopt the D03 curve (that extends out to a larger distance) after scaling it to match the M06 curve at 8 kpc.

For the direction of the LW, D03 predict that the bulk of absorbing material lies in front of 6 kpc after which A_V levels off to 3.8; this includes a ~10%-contribution from material that lies mainly beyond 10 kpc. However, for $|l| < 20°$ the underlying dust model is not accurate. The A_{Ks} extinction maps by Marshall et al. (2006) (M06), available for $|l| < 100°$, $|b| < 10°$ at 15′-resolution and computed out to ~9 kpc, are derived by comparing the colors of a simulated stellar population with the corresponding observed 2MASS colors in a given direction. The predicted extinction towards the LW is somewhat higher than the value from D03 ($A_V = 3.9$ at 8 kpc for M06 versus $A_V = 3.5$ for D03), although both curves have similar shapes. For the total integrated extinction $A_{V,\mathrm{max}}$, we will adopt the value from D03 that is scaled to match A_V from M06 at 8 kpc, i.e. $A_{V,\mathrm{max}} = 4.2$; this corresponds to a neutral-hydrogen column density $n_{H,\mathrm{max}} = 7.6 \ 10^{21}$ cm^{-2} (Predehl & Schmitt 1995). We use coefficients from Sirianni et al. (2005) to convert A_V to extinction values in the *HST* filters: $A_{B_{435}} = 1.316 A_V$, $A_{R_{625}} = 0.851 A_V$ and $A_{\mathrm{H}\alpha} = 0.815 A_V$.

Besides the uncertainty in $A_{V,\mathrm{max}}$ and the distance dependence of the extinction, spatial variations as function of longitude and latitude also complicate matters. Owing to the weak age- and metallicity-dependence of their luminosities and colors, red-clump giants have frequently been used to trace extinction variations in the bulge (see for example Stanek et al. 1997). Fig. 2 shows CMDs for each of the chips of the ACS mosaic (4 pointings, 2 chips per pointing) with the red-clump giants visible in the upper right. The variation of their location implies that there are significant variations in the extinction, especially in the east-west direction, that amount to a maximum variation of ~1 mag in R_{625}. This corresponds to a ~30% variation in A_V compared to $A_{V,\mathrm{max}} = 4.2$.

3.4. *X-ray spectral properties*

All *Chandra* sources in the ACS field but one are detected with fewer than 100 counts (the brightest source, our CV candidate LW 1 (§4.1.1), has 152 net counts); since this precludes the use of spectral fitting, we resort to quantile analysis (Hong et al. 2004) to derive the X-ray spectral properties. In brief, quantile analysis constrains the spectral parameters and
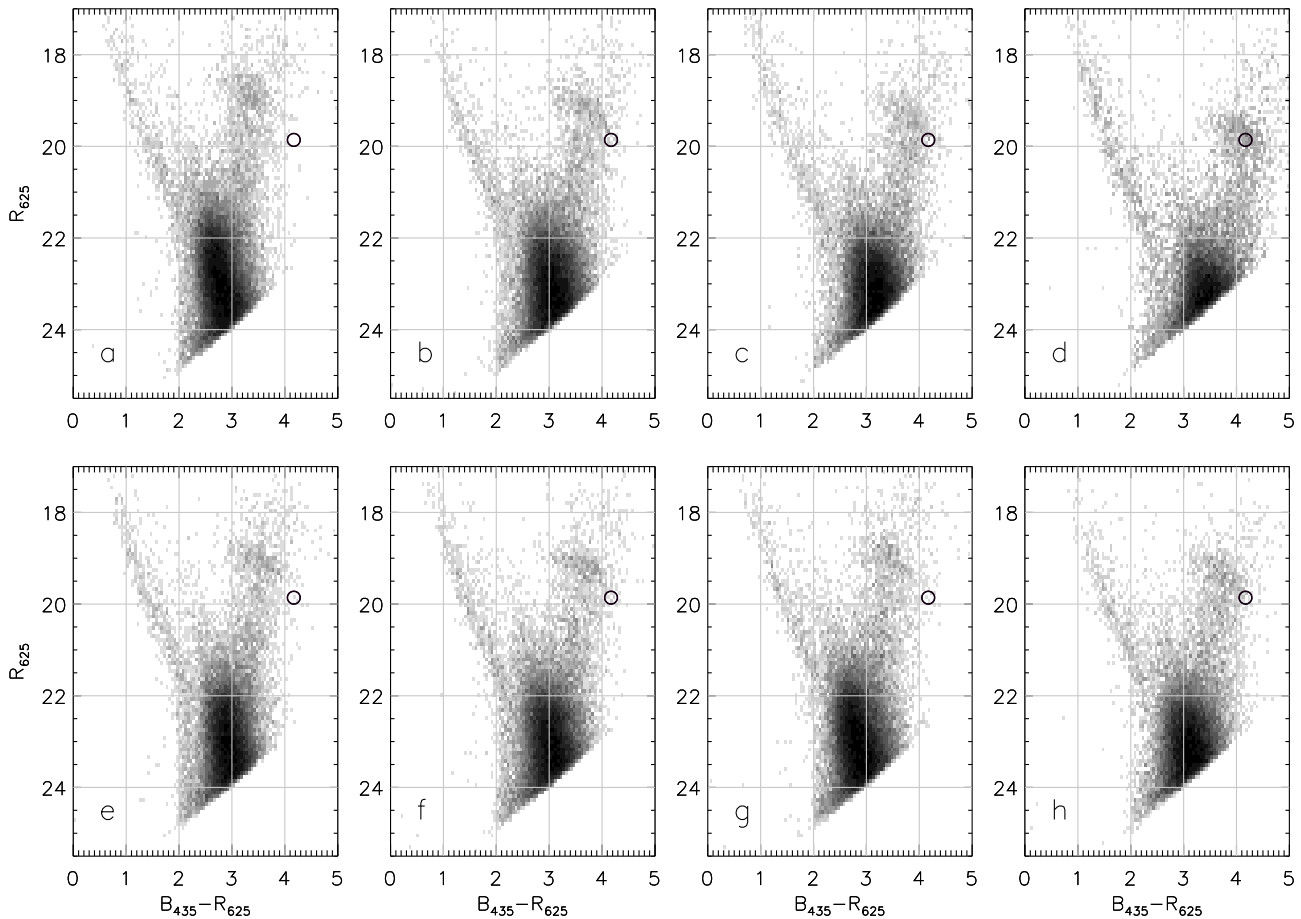
FIG. 2.— Color-magnitude diagrams extracted from each of the eight chips of the ACS mosaic illustrate the variation of A_V in our field. The panels a to h are arranged according to their relative location on the sky (so, panels a and h correspond to the north-east and south-west corner of the mosaic, respectively). The density of stars in each bin is indicated with a logarithmic gray scale. The location of the red clump in panel d at $(B_{435} - R_{625}, R_{625}) \approx (4.2, 19.9)$ is marked with a circle in each panel. The variation of the observed locations of the red-clump giants between panels, as well as the location of the bulk of the stars, implies that the extinction A_V varies by ~30% across the field of the ACS mosaic.

column density from comparing the observed energy quantiles to those expected for a spectral model of choice; in the *ChaMPlane* analysis, we use the 25%, 50% and 75% energy quantiles. Sources are plotted, together with model grids, in a color-color plot from these three quantiles as shown in Fig. 3.

Since measurement errors on the quantiles of individual sources sometimes allow a broad range of parameters, we divide the sources in three spectral groups and assign to all sources of a given group one spectral model and n_H based on the quantiles of their stacked counts. H09 describe in detail the process of assigning spectral groups. The H09 spectral classification that we use in this paper is represented in Fig. 3. For the soft sources (group 1), we assume that the spectra can be characterized by a 1-keV MeKaL model which describes X-ray emission of an optically-thin hot plasma, appropriate for the coronal emission of normal late-type stars; the maximum $n_{H,\max}$ along the line of sight (§3.3) is adopted. For the hard group (2) we use the spectral parameters from H09 with a small adjustment, viz. instead of the quantile-based n_H, we also use $n_{H,\max}$ (~4% difference). Parameters for the absorbed group (3) are taken from H09 without adjustment. The parameters for each spectral group are summarized in Table 2. To minimize the effect of an incorrect choice of n_H (not all sources are seen through the maximum column density along the line of sight) we avoid using fluxes in the soft band. Since not all sources are detected in the hard band ($H_c = 2 - 8$ keV),

TABLE 2
SPECTRAL PARAMETERS FOR QUANTILE SPECTRAL GROUPS

Group	Model	Parameter	n_H $(10^{22}$ atoms cm$^{-2})$
1	MeKaL	$kT = 1$ keV	0.76
2	power law	$\Gamma=1.28$	0.76
3	power law	$\Gamma=1.21$	1.95

we compromise by working with broad-band ($B_x = 0.3 - 8$ keV) fluxes. For the B_x band, the countrate-to-(unabsorbed flux) conversion factor is 2.2 10^{-11} ergs cm^{-2} count^{-1} for group 2, while it is 16% (46%) higher for group 1 (3).

3.5. *Boresight correction and optical identification*

We improve the absolute astrometry of the *Chandra* positions in the ICRS (90%-uncertainty is 0.6″) by identifying likely matches between X-ray and optical sources. For this initial search for counterparts we use the search area inside a combined (i.e. X-ray/optical) ~95% error radius that is the quadratic sum of the 95% X-ray error circles (r_{95}) and 2× the error on the optical positions σ_o (defined in §3.2)[3]. We accept

---

[3] Since σ_o itself is the quadratic sum of the errors in the directions of right ascension and declination, 2 σ_o represents a 98% error radius if the errors on the optical positions are distributed as a 2-dimensional Gaussian. This
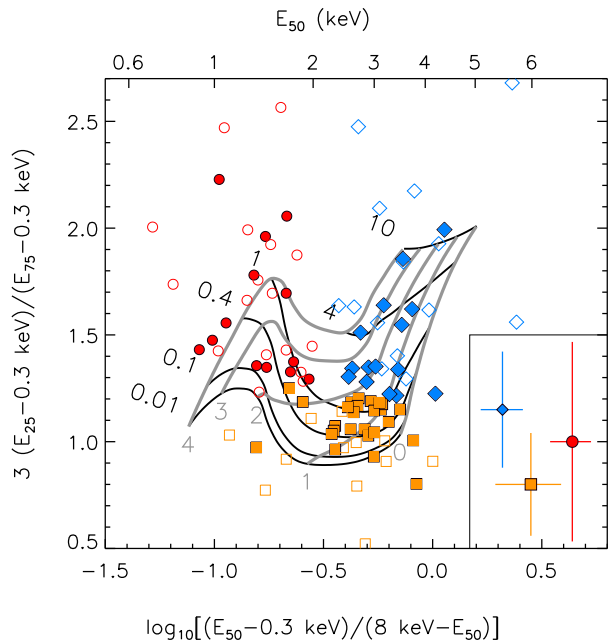
FIG. 3.— Quantile color-color diagram showing the *Chandra* sources in the ACS field and their X-ray spectral classification. For reference, we plot a grid for a power-law spectral model. The spectral properties of a source can be derived from its location with respect to the grid: black lines indicate contours of constant n_H while the power-law photon index Γ is fixed along the thick gray lines. The labels indicate the values of Γ and n_H (in units of 10^{22} cm^{-2}). Sources in the three spectral groups are plotted with (red) circles (group 1; relatively soft sources), (orange) squares (group 2; relatively hard sources) and (blue) diamonds (group 3; absorbed sources). See Table 2 for the group-specific spectral parameters. Sources with more and fewer than 15 net counts (B_x) are plotted with filled and open symbols, respectively. The median energy E_{50} can be read off from the top axis. The average errors for sources with ≥ 15 net counts are shown in the inset on the bottom right for each spectral group. *See the electronic edition of the journal for a color version.*

an optical source as a likely counterpart if it has unusual optical colors (blue, red and/or with an Hα excess with respect to the bulk of optical sources with similar magnitudes) or if it has optical and X-ray colors and an X-ray–to–optical flux ratio consistent with normal foreground stars (only if there are no other contenders in the error circle). To establish if the colors of a candidate counterpart are unusual, we examine its location in a CMD that includes stars from just a small (5″× 5″) region around the source since variations in the extinction can make a star appear bluer or redder when the bulk of the comparison stars are seen through a different extinction. We also include matches with OGLE-III variables (A. Udalski, private communication) that can be unambiguously identified in the *HST* images and are unsaturated (saturation hampers the determination of accurate optical positions); the properties of these variables are the topic of a forthcoming paper.

After the first round of matching, an initial boresight is determined from the weighted (by $1/r_{95}^2$) average of the X-ray minus optical positions of the likely matches. A uniform offset is determined for all four ACS pointings since their astrometries have been put on the same system; this is verified by examining the area where the pointings overlap. After correcting the X-ray positions for the boresight, the matching is

means that our search area combines 95% X-ray error radii with 98% optical error radii, where in practice the values for the former are at least 1.7 larger than the latter. Since the exact shapes of the underlying distributions of the positional errors are very difficult to measure, we choose not to refine this small discrepancy in "probability radii".

repeated after including in the search radius a contribution from the boresight error, i.e. we add a term (in quadrature) that equals 2× the error on the boresight. The resulting boresight between the original *Chandra* positions and the corrected *HST* astrometry is almost negligible: $\Delta\alpha = -0.02'' \pm 0.05''$, $\Delta\delta = +0.05'' \pm 0.04''$ (based on 11 matches).

4. RESULTS

At least one astrometric optical match is found for each of the 100 *Chandra* sources. Eleven sources have just 1 candidate counterpart inside the search radius, while 10 sources have 2, 17 have 3, and 62 have 4 or more candidate counterparts. The average search radius is $0.67''$. In some cases, a bright star in or near the error circle significantly reduces the sensitivity to detect counterparts. We mainly consider the optical colors of the candidates, together with the ratio of the X-ray and optical fluxes ($f_{B_x}/f_{R_{625}}$ or f_X/f_R in brief) and the X-ray spectral properties to constrain which of them (if any) is the most likely counterpart. We present cases that we have identified as likely and possible CVs (or other accreting binaries) in §4.1. Additional identifications are briefly discussed in §4.2; the main purpose here is to compare the X-ray properties of the candidate CVs with those of other source classes. Constraints on the nature of the hard point sources in the LW are discussed in §4.3.

4.1. *Candidate accreting binaries*

4.1.1. *Selection based on optical colors*

Most known CVs have blue colors that arise from the accretion disk, the accretion stream or sometimes the white dwarf, and show Balmer emission lines from the disk or stream. Therefore, if a *Chandra* source can be matched with a blue optical source that also has excess Hα flux, the source is a good candidate for being a CV. Based on this criterion, we initially find four good candidates, LW 1 to LW 4, whose properties are summarized in Table 3. Figs. 4 and 5 show their locations in the R_{625} versus $B_{435}-R_{625}$ and R_{625} versus H$\alpha-R_{625}$ CMDs and $B_{435}-R_{625}$ versus H$\alpha-R_{625}$ CCD ((red) diamonds); for comparison, we also include the other optical sources in all four ACS pointings. In the LW, however, where we observe sources at various distances and thus through a range of foreground extinctions, the interpretation of optical colors is not straightforward: a distant CV can be confused with a nearby late-type star. To demonstrate this, first we compare the expected colors for CVs to the colors of LW 1 to LW 4. Using the synphot package, we have simulated the colors for a spectrum with a flux-wavelength dependence $F \propto \lambda^{-2/3}$, i.e. appropriate for the emission from an accretion disk (Warner 1995). The grid in Fig. 5a shows how these synthetic colors behave as a function of reddening $E(B-V)$ and equivalent width (EW) of the Hα line. For this particular spectrum and the maximum reddening towards the LW ($E(B-V)_{max} = A_{V,max}/3.1 \approx 1.35$), no CVs are expected with $B_{435} - R_{625} \gtrsim 1.2$. However, small-scale variations in the extinction or different assumptions for the underlying optical spectrum (for example, an additional contribution from the light of the secondary) can explain redder systems like LW 1 and LW 3. To illustrate the spread in intrinsic colors of real CVs, we have plotted in Fig. 5a with small gray circles the colors of CVs[4] from the Sloan Digital Sky Survey

[4] Colors were computed using synphot and the SDSS spectra from Data Release 7. A small fraction (3.2% of the total area) of the F435W filter band-

TABLE 3
Candidate accreting binaries in the LW selected on optical colors

(1) ID	(2) CXOPS J	(3) Counts	(4) E_{50} (keV)	(5) Group	(6) α_{2000} (h m s)	(7) δ_{2000} (° ′ ″)	(8) R_{625}	(9) B_{435}	(10) Hα	(11) Log(f_X/f_R)	(12) Log(f_X/f_R)$_u$	(13) Comment
LW 1	175120.9−293318	152±14	3.0±0.2	2	17 51 20.910	−29 33 18.45	23.76	25.44	23.47	1.37(4)	0.07(4)	...
LW 2	175118.1−293332	9±5	1.5±0.3	1	17 51 18.177	−29 33 32.28	21.37	22.97	20.82	−1.3(2)	−2.1(2)	dMe star?
LW 3	175124.1−293738	14±6	1.8±0.3	2	17 51 24.123	−29 37 39.00	22.30	24.06	22.07	0.53(6)	−0.78(6)	...
LW 4	175140.0−293557	76±10	2.9±0.3	1	17 51 40.019	−29 35 57.60	23.81	25.03	23.36	0.0(2)	−0.8(2)	...
LW 5	175135.6−293754	19±6	3.3±0.7	2	17 51 35.679	−29 37 55.51	23.82	...	23.57	0.5(1)	−0.8(1)	...
LW 6	175122.8−293514	12±5	1.1±0.3	2	17 51 22.805	−29 35 14.28	22.82	25.29	22.45	−0.1(2)	−1.4(2)	...
LW 7	175111.8−293259	45±8	3.7±0.2	3	17 51 11.839	−29 32 59.74	23.56	26.6	23.25	0.87(8)	−2.64(8)	...
LW 8	175118.7−293811	32±7	3.5±0.4	3	17 51 18.788	−29 38 11.23	22.66	25.51	22.41	0.3(1)	−3.2(1)	...
LW 9	175118.5−293732	15±6	3.1±0.3	3	17 51 18.555	−29 37 32.14	23.92	26.9	23.66	0.5(2)	−3.0(2)	...
LW 10	175115.8−293802	7±5	2.7±1.6	2	17 51 15.856	−29 38 03.30	23.37	26.7	22.93	−0.1(3)	−1.4(3)	...
LW 11	175134.8−293809	36±7	3.6±0.3	3	17 51 34.849	−29 38 09.86	23.19	26.0	22.94	0.61(9)	−2.90(9)	...
LW 12	175141.4−293508	16±6	2.3±0.9	2	17 51 41.461	−29 35 08.65	22.82	24.93	22.65	−0.0(2)	−1.3(2)	...
LW 13	175142.8−293734	3±4	...	1	17 51 42.924	−29 37 35.80	24.51	27.1	24.22	−0.5(7)	−1.3(7)	...

Properties of our best candidate CVs (LW 1–4) and the more marginal candidates (LW 5–13). Column 1 gives the source name adopted in this paper whereas column 2 gives the official *Chandra* source name. Column 3 gives the net source counts in the B_x band (0.3–8 keV), followed by the median energy E_{50} in that band and the quantile spectral group. Optical positions (columns 6 and 7) are given in units of hours, minutes, and seconds (for the right ascension) and degrees, arcminutes, and arcseconds (for the declination); errors in the absolute astrometry are ~0.095″. The remaining columns list the magnitudes, the ratios of the observed (log(f_X/f_R)) and intrinsic (log(f_X/f_R)$_u$) X-ray and optical fluxes, and comments. Fluxes are corrected for extinction using the group-specific n_H values listed in Table 2. Quoted errors in the flux ratios only include a contribution from errors in the X-ray counts, not from systematic errors. Errors are given in parentheses as the (uncertainty) in the last digit.

(SDSS; Szkody et al. (2002) and follow-up papers) that lie at $|b| \geq 55°$ and are therefore not or moderately reddened (the total Galactic extinction in the direction of these systems is only $0.02 \lesssim A_V \lesssim 0.13$; D03). The location of the unreddened main sequence (gray line) shows how our color selection of CV candidates can cause confusion with nearby M dwarfs—also common X-ray sources. The color grid for an M0 dwarf in Fig. 5b shows this in more detail; for example, the optical colors of LW 4 could point at a CV with $E(B-V) \approx 1.4$ and EW(Hα) $\approx$ 30–40 Å, but can also be explained by an M2–3 dwarf with $E(B-V) \approx 0$ and EW(Hα) ≈ 10 Å. LW 4 is unlikely to be of later spectral type since the source is too blue, or of earlier type which would require that EW(Hα) $\gtrsim 15$ Å. In the spectroscopic study of X-ray–selected M-dwarfs by Mochnacki et al. (2002), EW(Hα) does not exceed 11 Å among the 54 stars in the sample.

We try to resolve this ambiguity by considering other properties, too. For LW 1, LW 3 and LW 4 the ratio of the intrinsic X-ray to optical flux, log(f_X/f_R)$_u$, exceeds -1 if we assume that they are seen through $n_{H,\mathrm{max}} = 7.6 \, 10^{21}$ cm^{-2} (Table 3, column 12), and is even higher (> 0) if they are in fact nearby and therefore unabsorbed (Table 3, column 11; see §4.1.2 for details on estimating (f_X/f_R)$_u$). These inferred values of log(f_X/f_R)$_u$ are high compared to the typical range for active M dwarfs (see § 4.1.2). For LW 1 and LW 3, their classification as CVs is also the more plausible one on the basis of their X-ray colors; the quantile diagrams of Fig. 6 shows that their spectra are hard ($kT > 10$ keV or $\Gamma \lesssim 1$) which is unusual for stellar coronal sources. Also for LW 4, which is softer in X-rays, we favor the explanation as CV: if the star is indeed an unabsorbed M2 dwarf, the absolute V magnitude ($M_V = 9.9 - 10.2$; Carroll & Ostlie (1996); Bessell (1991)), and $V - R_{625}$ color (~0.84 as derived with synphot using a spectral standard) would put this star at a distance of ~7.2–6.3 kpc, which is inconsistent with the implied low reddening

pass is not covered by the spectra, which means that the actual $B_{435} - R_{625}$ colors of the SDSS CVs are slightly bluer than plotted in Fig. 5a.

from Fig. 5b. The case of LW 2 is less clear. If the source is an M5 dwarf with EW(Hα) ≈ 10 Å (see Fig. 5b), its distance would be ~250–700 pc ($M_V = 12.3 - 14.7$; $V - R_{625} \approx 0.8$) and thus $E(B-V) \approx 0.1$ which is roughly consistent with the estimated $E(B-V)$ from the color-color grids (Fig. 5b). Moreover, log(f_X/f_R)$_u < -1$, and the soft X-ray colors are more typical for coronal than accreting sources. On the other hand, dwarf novae in outburst can have soft X-ray spectra (see for example Wheatley et al. 1996). Such a state is often accompanied by weak Balmer emission lines or even absorption lines as the accretion disk becomes optically thick. We cannot determine if LW 2 also displayed this behavior. The X-ray photons from LW 2 mainly come from the second ACIS exposure taken 3 days after the *HST* observation (the source was not detected separately in the other two ACIS exposures). We conclude that of our four blue and Hα-excess sources, LW 1, LW 3 and LW 4 are likely CVs while LW 2 is a possible CV or a dMe star. Fig. 7 shows their finding charts.

Nine additional *Chandra* sources are matched with Hα-excess sources. These are marked with (green) squares in Figs. 4, 5 and 6ab and included in Table 3 as LW 5 to LW 13. We note that LW 6 and LW 12 have a relatively bright neighbor ($R_{625} \approx 17$) at a separation of 0.6″ and 0.5″ (~13 and 10 pixels), respectively, which may have affected their photometry. On the other hand, their PSFs look clearly separated and the photometric quality flags do not signal any problems. We consider these nine sources as less secure CV candidates as LW 1, 3 and 4 because most are not or only slightly blue compared to the bulk of the optical sources; others have $S/N < 5$ in B_{435} or are not detected in B_{435} at all. While this is perhaps more suggestive of them being late-type stars rather than CVs, we still mention them for two reasons. First, some CVs do not appear blue in $B - R$ (the dwarf nova identified with the *Chandra* source CX 1 in the globular cluster M 55 is an example; see Bassa et al. (2008)). And second, the X-ray colors (and for LW 5 also the (f_X/f_R)$_u$ ratio) of some of these sources are too high for normal or coronally-active stars, see Figs. 6a and b. Not much can be said about the X-ray colors of
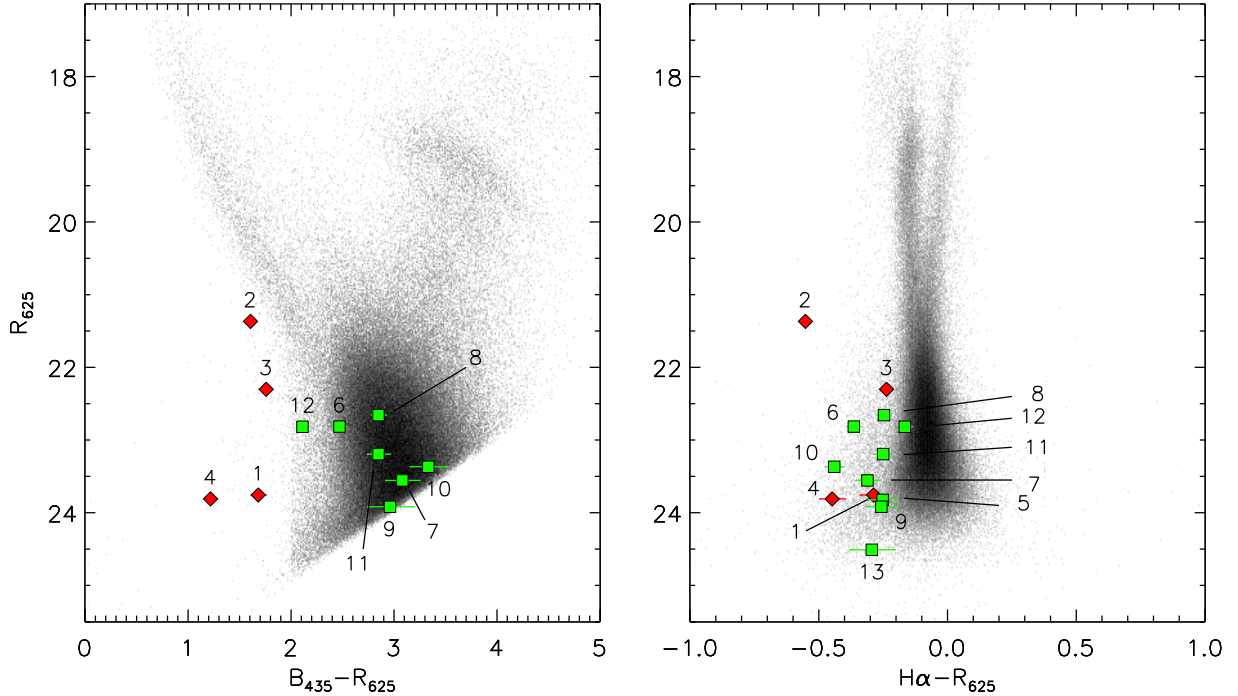
FIG. 4.— Color-magnitude diagrams with the candidate CVs from Table 3 indicated with (red) diamonds (LW 1–4; best candidates) and (green) squares (LW 5–13; possible CVs). Error bars are plotted but in some cases are comparable to the size of the symbols. Candidates for which $S/N < 5$ in B_{435} are not plotted in the left panel. The density of stars in the CMDs is indicated with a logarithmic gray scale; optical sources from all four ACS pointings are included. *See the electronic edition of the journal for a color version.*

LW 6, LW 10 and LW 13 that are detected with fewer than 15 net counts, while the spectra of LW 7, LW 8, LW 9 and LW 11 appear absorbed with $n_H \gtrsim 10^{22}$ cm^{-2} ($A_V \gtrsim 5.6$). This requires some source of extra extinction, for example originating inside a binary system or provided by the host galaxy of an active galactic nucleus (AGN). In the latter case the Hα excess could be explained in the relatively unlikely event that an emission line happens to be redshifted in the F658N band. For coronal sources such high n_H values are not expected. Occasionally, the column density is enhanced when a star undergoes a large coronal flare but these cases are rare and not yet fully understood (Güdel 2004).

4.1.2. *Selection based on f_X/f_R ratios*

It is well-known (e.g. Stocke et al. 1991; Krautter et al. 1999) that the distribution of the ratio of intrinsic X-ray to optical fluxes (f_X/f_{opt})$_u$ for accreting binaries extends to significantly higher values than for coronal sources, whereas it largely overlaps with the range observed for galaxies. The CVs in Verbunt et al. (1997) have $\log(f_X/f_V)_u$ between -2.4 and $+0.5$ where we converted from their 0.5–2.5 keV band to our B_x band using the 2-keV thermal-bremsstrahlung model used in Verbunt et al. (1997). On the other hand, for the nearby stars in Schmitt & Liefke (2004) and the active binaries in Dempsey et al. (1993) and Dempsey et al. (1997), $\log(f_x/f_V)_{u,max} \approx -1$ in the ROSAT band which, for the X-ray spectra typical for coronal sources ($kT \approx 1$ keV), would give a similar value in our B_x band. Krautter et al. (1999) find $< \log(f_X/f_V)_u > = -1.33 \pm 0.50$ for dMe stars (that have the highest flux ratio's among single stars) with only a few outliers that have $\log(f_X/f_V)_u > -0.5$. Therefore, even in the absence of any optical matches with distinct colors, we can iden-

TABLE 4
CANDIDATE ACCRETING BINARIES IN THE LW SELECTED ON $(f_X/f_R)_u$

ID	CXOPS J	Counts	E_{50} (keV)	Log(f_X/f_R) (minimum)	Log$(f_X/f_R)_u$ (minimum)
LW 14	175127.9−293508	14±5	2.4(6)	0.9(2)	−0.4(2)
LW 15	175119.1−293740	41±8	3.1(6)	1.66(9)	0.36(9)
LW 16	175127.0−293706	46±8	2.6(5)	1.37(8)	0.06(8)
LW 17	175130.0−293613	88±11	2.9(3)	0.94(5)	−0.37(5)
LW 18	175114.2−293224	22±7	3(1)	1.1(1)	−0.2(1)
LW 19	175133.6−293313	77±10	3.1(2)	0.50(6)	−0.81(6)
LW 20	175130.7−293232	54±9	3.2(3)	0.65(7)	−0.65(7)
LW 21	175120.7−293417	18±6	3.8(9)	0.4(1)	−0.9(1)
LW 22	175124.0−293532	13±5	1.2(7)	0.6(2)	−0.7(2)
LW 23	175139.6−293811	34±7	2.3(5)	0.5(1)	−0.8(1)
LW 24	175128.9−293412	14±6	2.7(7)	0.6(2)	−0.7(2)
LW 25	175123.5−293755	38±8	3.0(4)	0.3(9)	−1.0(9)

For each source we give the name adopted in this paper, followed by the official source name, the net counts in the B_x band, the median energy in B_x, and the ratio of X-ray and optical fluxes computed for the brightest optical source in the error circle (observed: $\log(f_X/f_R)$; unabsorbed: $\log(f_X/f_R)_u$). All sources have quantile spectral group 2; optical and X-ray fluxes are therefore dereddened with $n_H = 7.6 \ 10^{21}$ cm^{-2}. Quoted errors in the flux ratios only include a contribution from errors in the X-ray counts, not from systematic errors. Errors are given in parentheses as the (uncertainty) in the last digit.

tify CV (or AGN) candidates among the *Chandra* sources by considering the minimum value of $(f_X/f_R)_u$ that results from the brightest optical source in the search area. The difficulty of applying this diagnostic to our sample is that we only have a rough estimate of the extinction that is needed to convert between observed and intrinsic fluxes. We adopt the quantile-group specific n_H values (Table 2) but stress that this is only
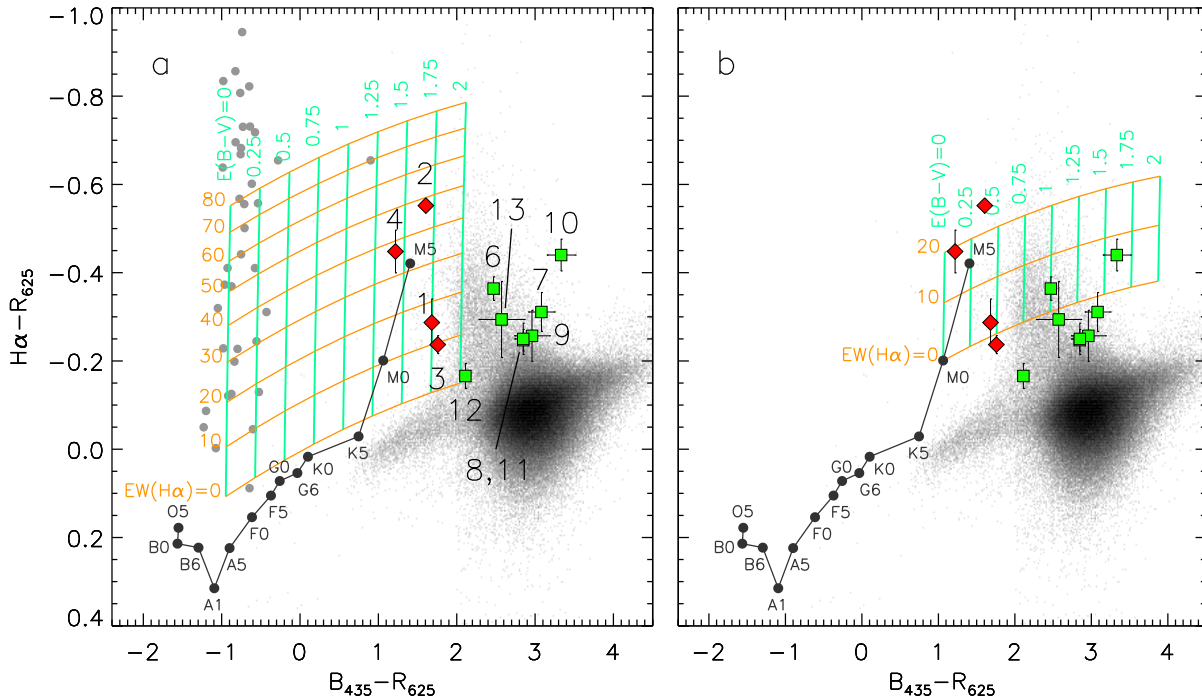
Fig. 5.— Color-color diagrams with the candidate CVs from Table 3 marked with (red) diamonds (LW 1–4; best candidates) and (green) squares (LW 5–13; possible CVs), and the location of the unreddened main sequence (computed with spectral standards from Jacoby et al. (1984)) plotted as a dark-gray line. The grids show how the synthetic colors for a disk spectrum (*a*) and an M0-dwarf spectrum (*b*) vary as function of reddening $E(B - V)$ (in steps of 0.25 mag) and the equivalent width of Hα (in steps of 10 Å). Grids were computed with the `synphot` package; we assumed that the Hα emission line has a Gaussian profile with a full width at half maximum of 25 Å for the disk model, and 1.5 Å for the M0-dwarf model. The small light-gray circles in panel *a* are the colors of SDSS CVs at $|b| > 55°$ and illustrate the (spread in the) colors of real CVs. The location of optical sources detected in all four ACS pointings is shown with a logarithmic gray scale. *See the electronic edition of the journal for a color version.*

an estimate. For example, if the fluxes for a source in group 1 are corrected for $n_H = 7.6\ 10^{21}$ cm^{-2} whereas in reality $n_H = 0$, $\log(f_X/f_R)_u$ would be underestimated by 0.8 dex. Similarly, the $\log(f_X/f_R)_u$ value for a group-2 source could be up to 1.3 dex too small, although the situation is likely not that serious as their distribution indeed appears to be concentrated between $n_H \approx 4\ 10^{21}$ and 10^{22} cm^{-2} in Fig. 3. For group-3 sources, for which both n_H and the underlying spectra are poorly constrained, $\log(f_X/f_R)_u$ is even more difficult to estimate. We further assume that $f_V \approx f_R$, to facilitate comparison with the literature. We convert our optical magnitudes to fluxes using the zero points from Sirianni et al. (2005) and apply a small correction factor to specify fluxes in a 1000-Å–wide band width[5], also to make comparison with published values easier.

Based on the above ranges, we select possible CVs as sources with $\log(f_X/f_R)_{u,\mathrm{min}} \gtrsim -1$. The twelve sources (besides LW 1, 3, 4 and 5) that satisfy this criterion are listed in Table 4 and marked in the quantile diagrams of Fig. 6a and b ((blue) circles). The relatively hard spectra support their classification as non-coronal sources. However, both their quantile and $(f_X/f_R)_u$ values prevent the distinction from AGN, and the colors of the astrometric optical matches do not put additional constraints on the source classifications. Possibly,

the true optical counterparts are too faint to be detected. The detection limit of $R_{625} \approx 26.7$ implies that any undetected counterparts have $\log(f_X/f_R)_{u,\mathrm{min}} = 0.2 - 0.9$ for the sources in Table 4, which would be consistent with accreting binaries.

4.2. Other identifications

We defer a detailed discussion of stellar coronal sources in the LW to a follow-up paper, but for the purpose of putting the X-ray properties of our candidate CVs into a broader context we also briefly discuss likely coronal sources here. Two sources are matched with bright UCAC2 stars. Our low-resolution optical follow-up spectra show them to be a K and F star. Since these stars are heavily saturated in the ACS images, it is impossible to look for other optical sources in the error radius. In the field of view of the ACS images, stars of this brightness are however rare and chance alignments are unlikely. Other likely coronal sources are found among astrometric matches of *Chandra* sources to OGLE-III variables (A. Udalski, private communication); while we have not done a test yet to estimate how many of the thirteen OGLE matches could be spurious, a detailed analysis of matches between the *Chandra* sources in the two other Windows with OGLE-II variables (van den Berg et al. 2006) showed that <10% are expected to be random. Also, twelve of the light curves vary periodically and suggest binary periods from 0.36 days to 34 days. This could explain the X-rays as being generated by tidally-induced rapid rotation. The UCAC2 stars (LW 26 and 27) and the variables (LW 28–40) are plotted with (orange) circles in Figs. 6c and d for sources with >15 net counts. They are predominantly soft in X-rays but we note the rela-

[5] To compute the optical flux f_R, we multiply the flux density by the filter width for which we adopt the often-used value of 1000 Å instead of ~415 Å, which is the actual width the F625W filter. The correction factor that we add to the measured $\log(f_X/f_R)$ and $\log(f_X/f_R)_u$ ratios is therefore $\log(\frac{1000}{415}) = 0.38$.
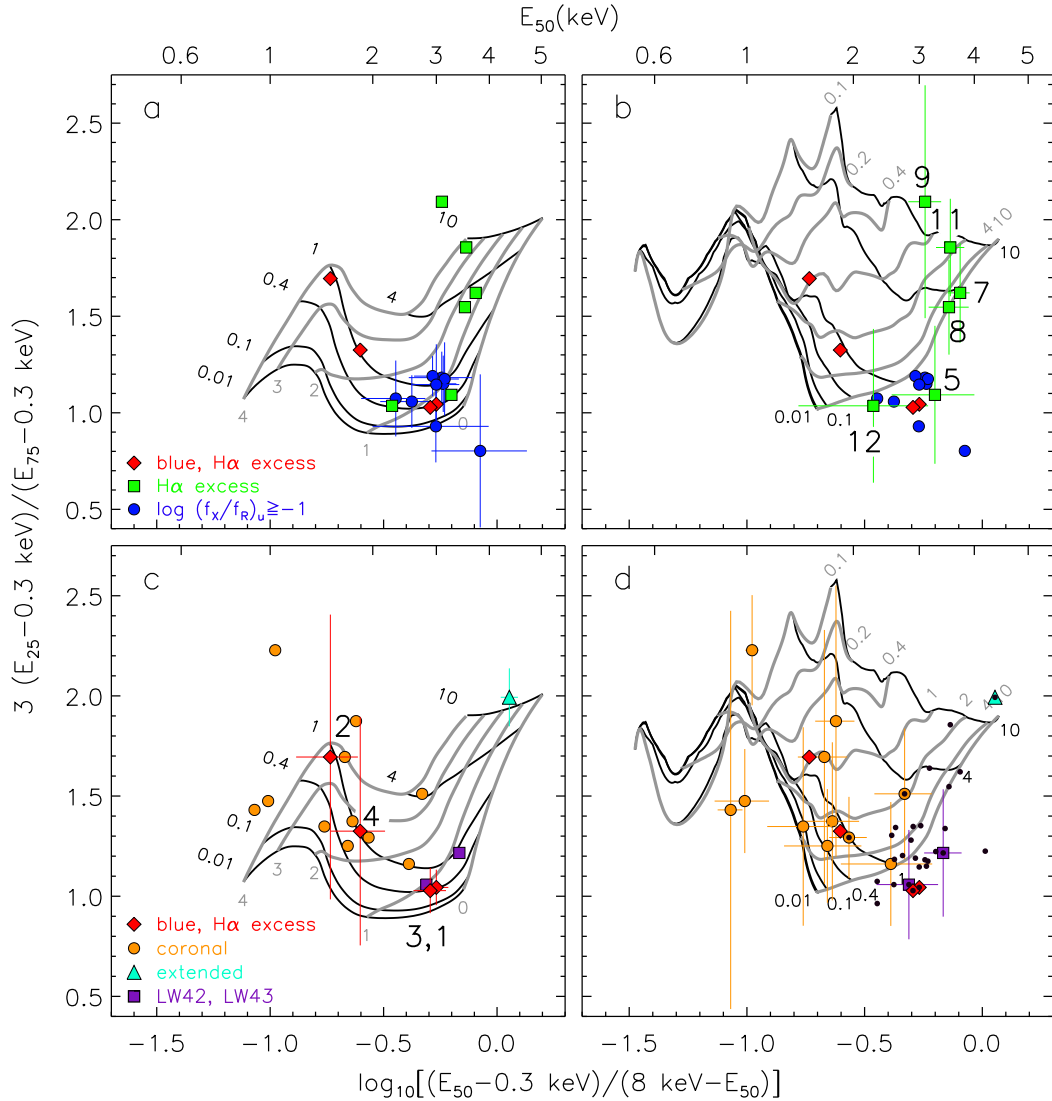
Fig. 6.— Quantile color-color diagrams with our best candidate CVs LW 1–4 marked in each panel with (red) diamonds and labelled in panel *c* only. The model grids on the left (*a, c*) are computed for a power-law spectrum, while the grids on the right (*b, d*) are for a single-temperature MeKaL model. In panels *a* and *b*, we also include the other candidate CVs: (green) squares are the sources with Hα-excess fluxes (labelled in *b*) and (blue) circles the sources with $\log(f_X/f_R)_u \gtrsim -1$. In panels *c* and *d*, we include the identifications with coronal sources ((orange) circles) that are distinctly softer than most candidate CVs from *a* and *b*. Other noteworthy sources like the candidate AGN LW 41 ((cyan) triangle) and LW 43 ((purple) square) are also included in *c* and *d*. Error bars are plotted in one panel only for clarity. Thick gray lines are contours of constant temperature kT or photon index Γ; black lines are contours of constant n_H. Except for LW 2 and 3, sources with <15 net counts are omitted. The small black circles in panel *d* mark sources with $S/N_{H_c} > 3$ that are discussed in §4.3. *See the electronic edition of the journal for a color version.*

tively hard X-ray colors of LW 32 and LW 37. The derived n_H values are consistent with $n_{H,max}$ or lower, suggesting many may be foreground coronal sources. They occupy a distinctly different region of the quantile diagram than most candidate CVs from §4.1 (Figs. 6a and b). The properties of LW 26–40 are summarized in Table 5. For the *Chandra* sources that are matched to OGLE variables we list the optical ACS source that lies closest to the OGLE position[6]. In three cases, two optical sources lie at a similar distance and we give the co-ordinates, magnitudes and flux ratios of both. The relatively high $(f_X/f_R)_u$ ratios for the fainter of the two candidate identifications to LW 29 and LW 36 make them the less likely of the two candidate matches to these *Chandra* sources.

Another interesting identification is the red extended object

---

^{6} after correcting for a small systematic offset between the OGLE and ACS coordinate systems, computed using four unambiguous identifications

that matches with LW 41, see Fig. 8 and Table 5. Its position in the quantile diagram suggests that it is highly absorbed and that the spectrum is consistent with a power law with photon index 1–2 ((cyan) triangle in Figs. 6c and d). We suggest that this source is a type-II AGN, and that some sources in this region of the quantile diagram are too.

Finally, we draw attention to two relatively hard sources, LW 42 and LW 43, that both are matched to optical sources with remarkable colors but that cannot readily be classified ((purple) squares in Figs. 6c and d; Table 5). One of the candidate counterparts to LW 42 is detected in the B_{435} band but in neither the R_{625} nor the Hα images, and must therefore be very blue. The n_H, and therefore $\log(f_X/f_B)_u$, is not well-constrained. The source was assigned quantile-group 3 which gives $\log(f_X/f_B)_u \approx -3.5$. However, if we assume that the underlying spectral model is a power law, lower n_H values are
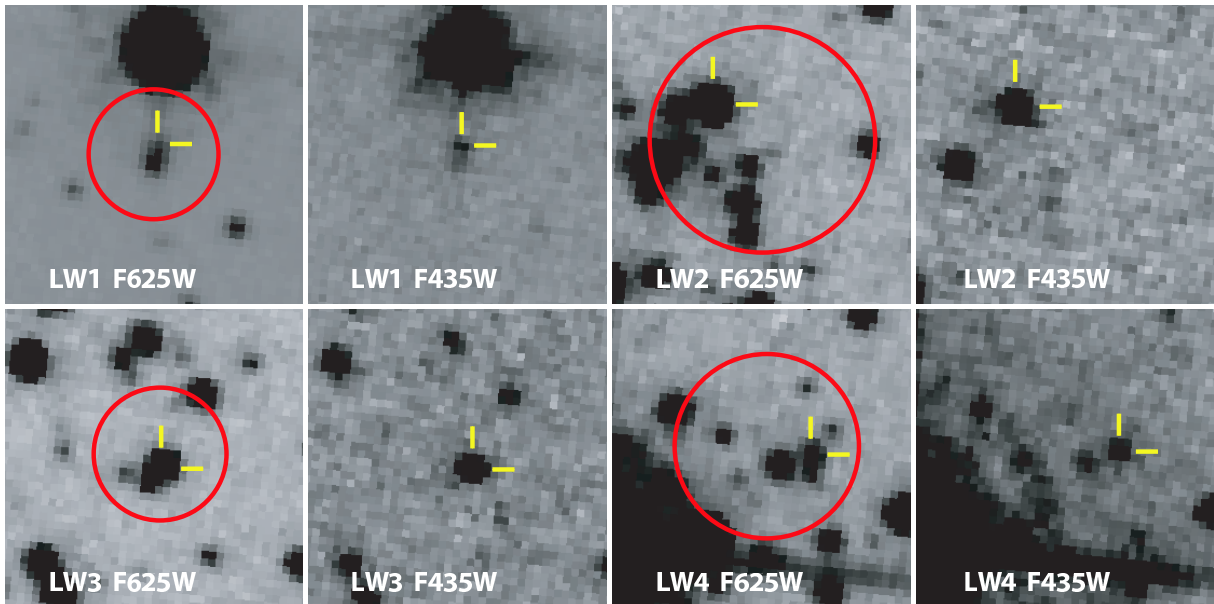
FIG. 7.— Finding charts in F625W and F435W for the four best candidate CVs. In the F625W images, we show the area inside which we search for optical counterparts with a (red) circle (with radius 0.44″ for LW 1, 0.76″ for LW 2, 0.45″ for LW 3 and 0.62″ for LW 4). The candidate CVs are indicated with (yellow) tick marks. The scaling of the images is adjusted to highlight the relatively blue color of the proposed counterparts. North is up, east is left. *See the electronic edition of the journal for a color version.*
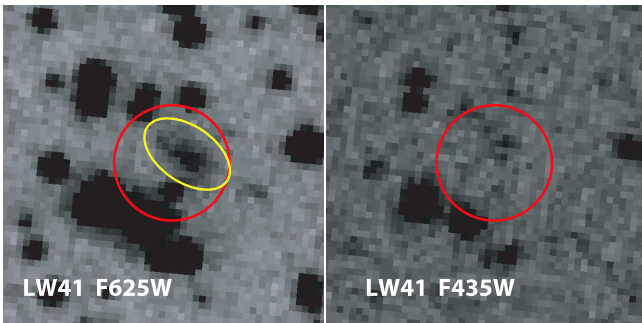

FIG. 8.— Finding charts in F625W and F435W of the region around LW 41. An extended and red object (indicated by (yellow) ellipse) lies near the center of the area inside which we search for optical counterparts marked with the (red) circle (radius 0.45″). North is up, east is left. *See the electronic edition of the journal for a color version.*

also allowed; for $n_H = 7.6 \ 10^{21}$ cm^{-2}, $\log(f_X/f_B)_u \approx 0.1$. The X-ray spectrum is too hard to be from a stellar coronal source. LW 43 has an exceptionally red optical source in the error circle which looks normal in $H\alpha - R_{625}$. The spectrum is harder than expected for a coronal source, and we suggest an obscured AGN is the most plausible explanation.

The remaining 57 LW sources that are not listed in Tables 3–5 do not have candidate counterparts with unusual colors, nor are the limits on their $(f_X/f_R)_u$ values stringent enough to exclude that they are normal or active stars. For sources with sufficient counts, the only distinction that can be made is between probable stellar coronal and non-coronal sources based on X-ray spectral hardness that (as Fig. 6 shows) are distinctly different for these two source classes.

4.3. *Constraints on the hard (2–8 keV) source population*

H09 use the number-density versus flux distribution ($\log N - \log S$) of *Chandra* sources in seven inner-bulge fields including the three Windows to study the hard point-source population and its radial distribution in the central region of the Galaxy. Their results suggest that the high concentration of hard sources around SgrA* is part of a population

that extends out to at least the LW where the hard-source density is still significantly elevated above the extra-galactic $\log N - \log S$ curve, in contrast to what is seen in Galactic-plane fields at larger offsets from SgrA*. Of the 109 LW sources with $S/N_{H_c} > 3$ that are used in the analysis by H09, 29 are covered by the ACS mosaic[7]. In Fig. 6d these are marked with black dots. The average flux limit for a $S/N_{H_c} = 3$ detection in the field of the ACS mosaic is $2 \ 10^{-15}$ ergs s^{-1} cm^{-2} (2–8 keV) for a power-law spectrum with photon index $\Gamma = 1.7$ absorbed by $n_{H,\mathrm{max}} = 7.6 \ 10^{21}$ cm^{-2}. Based on this limit and the high-latitude hard-source density from Kim et al. (2007), we expect that $\sim 17 \pm 4$ (Poisson errors only) hard sources are galaxies. We now consider what constraints we can set on the nature of the remaining, i.e. Galactic, sources based on our optical identifications.

Of the 29 sources, we have plausible identifications for six: two are identified with periodic OGLE variables and likely coronal sources (LW 32 and LW 33; these are among the "softest" hard sources), one is the extended object and probable AGN LW 41, one is the red object and candidate AGN LW 43, and two are our likely CVs LW 1 and LW 3. The hard X-ray spectra of the latter two could indicate they are magnetic systems that often have harder X-rays than seen in CVs of other types (e.g. Heinke et al. 2008). The properties of eleven sources appear to exclude a coronal nature: one is the blue source LW 42, seven sources have high values for $\log(f_X/f_R)_{u,\min}$ (LW 15–17, LW 19, LW 20, LW 23, LW 25), and three sources that are matched with $H\alpha$-excess objects (LW 7, LW 8, LW 11) are also unlikely to be coronal as they lie in quantile group 3, i.e. show indications of extra absorption in X-rays. As outlined in §4.1 and §4.2, these sources can be either accreting binaries or AGN. We have no obvious optical clues to the nature of the remaining twelve sources that all have at least one astrometric match with non-distinct colors. Since they lie to the right of most coronal sources in Figs. 6c and d, they are not likely to be normal or active stars. The

[7] One can look up the IDs of these sources in Table 1.

TABLE 5
Other identifications of *Chandra* sources in the LW

(1) ID	(2) CXOPS J	(3) Counts	(4) E_{50} (keV)	(5) Group	(6) α_{2000} (h m s)	(7) δ_{2000} (° ′ ″)	(8) R_{625}	(9) B_{435}	(10) Hα	(11) Log(f_X/f_R)	(12) Log(f_X/f_R)$_u$	(13) Comment
LW 26	175130.6−293227	38±8	0.91±0.07	1	17 51 30.598	−29 32 27.82	11.8[a]	...	...	−4.37(9)[a]	−5.21(9)[a]	UCAC2
LW 27	175128.1−293703	15±6	1.0±0.2	1	17 51 28.133	−29 37 03.37	12.2[a]	...	...	−4.6(2)[a]	−5.5(2)[a]	UCAC2
LW 28	175137.5−293602	29±7	1.03±0.04	1	17 51 37.533	−29 36 02.58	...	...	15.52	−3.0(1)[c]	−3.9(1)[c]	OGLE
LW 29[b]	175129.5−293602	16±6	1.7±0.3	1	17 51 29.555	−29 36 02.45	23.70	26.8	23.42	−0.1(2)	−0.9(2)	OGLE
...	...	...	...	...	17 51 29.548	−29 36 02.55	21.05	25.06	20.86	−1.2(2)	−2.0(2)	OGLE
LW 30	175118.9−293733	14±6	1.7±0.3	1	17 51 18.905	−29 37 33.65	21.05	24.81	20.86	−1.2(2)	−2.0(2)	OGLE
LW 31	175139.7−293546	9±5	1.3±0.4	1	17 51 39.765	−29 35 47.03	...	17.75	16.63	−3.0(2)[c]	−3.8(2)[c]	OGLE
LW 32	175136.4−293747	21±6	2.8±0.5	3	17 51 36.400	−29 37 47.50	18.51	22.04	18.34	−1.5(1)	−5.0(1)	OGLE
LW 33	175132.5−293636	46±8	1.9±0.2	1	17 51 32.528	−29 36 36.35	19.61	22.70	19.44	−1.27(8)	−2.07(8)	OGLE
LW 34	175119.1−293551	17±6	1.7±0.3	1	17 51 19.138	−29 35 51.52	20.07	23.73	19.95	−1.3(1)	−2.1(1)	OGLE
LW 35	175137.3−293409	15±6	1.8±0.2	1	17 51 37.307	−29 34 09.67	20.14	23.61	19.96	−1.6(2)	−2.4(2)	OGLE
LW 36[b]	175131.0−293216	17±6	1.7±0.4	2	17 51 31.065	−29 32 16.98	19.13	22.69	18.98	−1.5(2)	−2.8(2)	OGLE
...	...	...	...	...	17 51 31.065	−29 32 17.16	23.82	...	23.59	0.4(2)	−0.9(2)	OGLE
LW 37[b]	175114.5−293756	18±6	2.5±0.7	2	17 51 14.579	−29 37 56.18	22.65	25.64	22.49	0.0(2)	−1.3(2)	OGLE
...	...	...	...	...	17 51 14.565	−29 37 56.04	20.36	24.33	20.13	−0.9(2)	−2.2(2)	OGLE
LW 38	175133.2−293718	14±5	1.5±0.2	1	17 51 33.242	−29 37 18.59	19.43	21.73	19.30	−1.9(2)	−2.7(2)	OGLE
LW 39	175138.8−293409	18±6	1.4±0.3	1	17 51 38.886	−29 34 09.20	20.72	23.76	20.54	−1.2(2)	−2.0(2)	OGLE
LW 40	175138.3−293308	14±6	1.0±0.2	1	17 51 38.351	−29 33 09.18	18.08	19.18	18.14	−2.4(2)	−3.2(2)	OGLE
LW 41	175137.4−293515	61±9	4.4±0.2	3	17 51 37.485	−29 35 15.29	22.50	...	25.0	0.56(7)	−2.95(7)	extended
LW 42	175133.3−293430	30±7	3.4±0.3	3	17 51 33.317	−29 34 30.63	...	27.1	...	2.1(1)[d]	−3.5(1)[d]	blue
LW 43	175127.8−293510	28±7	2.8±0.5	2	17 51 27.893	−29 35 10.48	21.92	26.6	21.79	−0.1(1)	−1.4(1)	red

Properties of the identifications discussed in §4.2. See Table 3 for an explanation of the columns.
[a]LW 26 and LW 27 are saturated in our ACS images. In column 8 we give the UCAC2 magnitude from Zacharias et al. (2004) that is between V and R, and use it to compute the X-ray–to–optical flux ratios.
[b]The identification of the OGLE variable in the ACS image is ambiguous, therefore we list both candidate optical counterparts.
[c]The optical source is saturated in the F625W image; we assume R_{625}=Hα to compute the X-ray–to–optical flux ratios.
[d]The optical source is not detected in the F625W and Hα images; we use B_{435} to compute the X-ray–to–optical flux ratios.

true counterparts may be below the detection limit in each or at least one filter which prevents us from measuring colors. In summary, the only constraint we can set on the Galactic hard sources is that they are a mix of stellar coronal and accreting sources but are, not unexpectedly, dominated by the latter. We come back to nature of the hard-source population in §5.3.

5. DISCUSSION

Our search for CVs in the LW has resulted in three likely CVs (LW 1, LW 3, LW 4) and 22 candidate CVs (LW2, LW 5–25). In what follows we set constraints on the distances of the best candidates (§5.1), and discuss the CV space density in the bulge (§5.2). We consider our identifications in the context of hard X-ray sources in the central bulge in §5.3.

5.1. *Distance constraints for the CV candidates*

With the limited information we have on our candidate CVs, it is difficult to meaningfully constrain their distances. We adopt two methods. One approach is to estimate minimum distances based on the R_{625} and Hα magnitudes, using the empirical relation between the equivalent width of the Hβ emission line, EW(Hβ), and the absolute V magnitude of the accretion disk: EW(Hβ)=0.3 M_V^2+exp(0.55 (M_V−4)) for EW(Hβ) $\gtrsim$ 15 Å, and M_V $\lesssim$ +6 for weaker lines (Patterson 1984). A relatively safe upper limit for EW(Hβ) is EW(Hα). Comparing the spectroscopically-determined equivalent widths of Hα and Hβ in the SDSS CVs (Szkody et al. (2002) and follow-up papers), we find that the mean ratio EW(Hβ)/EW(Hα) is 0.58 with a standard deviation 0.38 in a sample of 197 spectra. CV candidates LW 1, 3 and 4 have EW(Hα) values between ∼10 Å and ∼38 Å as in-

ferred from their locations with respect to the grid in Fig. 5a. Assuming EW(Hβ) $\leq$ EW(Hα), it follows that M_V $\lesssim$ 6 for LW 1 and LW 3, and M_V $\lesssim$ 8.8 for LW 4. Taking into account the A_V curve from D03, we find that $d_{\min}$ is between 3.5 and 6.2 kpc if $V − R_{625} = 0$ or between 4.2 and 9.3 kpc if $V − R_{625} = 1$ although, given the scatter of ±∼1.5 around the EW(Hβ) − M_V relation, LW 4 can be as close as 2.7 kpc. This suggests our candidates are much farther away than the majority of known CVs in the field. There are a few caveats however. We have assumed that the systems are not internally absorbed; if internal absorption is present, we have overestimated the actual distances. Furthermore, our estimate for EW(Hα) relies on the choice of model for the optical spectrum for which we have assumed a power-law model. If instead the white-dwarf spectrum—typically with broad Balmer absorption lines—contributes significantly around Hα, our derived EW(Hα) will be underestimated (and the minimum distances overestimated). Also, the EW(Hβ) − M_V relation applies to systems with disks, and is not appropriate for magnetic systems in which no disks or truncated disks are formed.

Therefore, we also use another approach to constrain the distances of our candidate CVs, viz. we test the hypothesis that they are at similar distances than most known CVs. The compilation of CVs by Ak et al. (2008) shows that the majority of known CVs is closer than ∼2 kpc, therefore we ask: based on the local CV density, how many CVs do we expect in the volume limited by a distance $d = 2$ kpc and the field of view of the ACS mosaic? To answer this question, we integrate the CV density n_{CV} along the line of sight and assume that it varies as a function of distance according to the Galaxy model by Picaud & Robin (2004) (see next section for

more details). For a maximum distance of 2 kpc the model is dominated by the Galactic disk whereas the bulge is not relevant. The resulting number of CVs, regardless of the selection effects that these systems would be subjected to in order to be detected, is 0.18 and 0.54 for a local CV density $1\ 10^{-5}$ and $3\ 10^{-5}$ pc^{-3}, respectively (these values cover the range of densities found in recent studies, see e.g. Ak et al. (2008), Grindlay et al. (2005), Pretorius et al. (2007)). The probability to detect 3 or more nearby CVs when in fact ~ 0.54 are expected is low ($\lesssim 1\%$ for a Poisson distribution). Therefore we conclude that we have probed the CV population at larger distances.

5.2. *The CV density towards the bulge*

Since we can derive only crude distances for our candidate CVs, it is not possible to use them to compute the CV density towards the LW directly. Instead, we assume that outside the local neighborhood the ratio of the CV-to-stellar space density is the same as locally, and compare the number of CVs we expect to detect to the number we actually see.

We first calculate the number of stars in a volume enclosed by the $6.6'\times 6.6'$ field of the ACS mosaic and the maximum distance d_{max} at which we can detect the brightest CVs (38 kpc for M_V=+3, Patterson (1998)). We adopt the Galaxy model by Picaud & Robin (2004) which consists of two parts. The first is a multi-component exponential disk with a radial scale length of 2.35 kpc, vertical scale heights between 60 and 185 pc (depending on the age of the component) and a central hole with a scale length of 1.31 kpc. The second component is a triaxial bulge with a major axis of 1.82 kpc that is rotated with respect to the line connecting us and the Galactic Center by $\sim 11°$, and axis ratios 1:0.31:0.26. The central nuclear bulge is not included, but is not relevant here given the separation of the LW from the Galactic Center. Picaud & Robin (2004) assume that the distance to the Galactic Center is 8.5 kpc. The star densities are normalized such that the disk gives a local density of 0.145 stars pc^{-3} and that the bulge has 11.5 stars pc^{-3} in the center of the Galaxy. See Picaud & Robin (2004) for details of this model (sech^2 density profile and "Pad7.9" luminosity function). Integrating the star density along the line of sight gives a total of about $12\ 10^6$ stars. Assuming that throughout this volume the ratio of CVs to stars is the same as locally implies that there are ~ 800–2400 CVs in this volume (for a local CV density of $1\ 10^{-5}$ and $3\ 10^{-5}$ pc^{-3}).

We verify how well the number of stars predicted compares to the number observed. To account for the distance out to which stars of different masses can be detected, we fold the Galaxy model with the local luminosity function from Bahcall & Soneira (1980). We calculate the number of stars predicted between $V = 22$ and 24. By choosing this range, we avoid sampling the steep-sloped part of the luminosity function (that applies for bright stars) at bulge distances where the star density is highest. This would have the adverse effect of making the predicted number very sensitive to the assumptions for A_V. We neglect differences between the luminosity functions in V and R_{625} which we believe are modest: the stars that dominate the optical detections are F to K stars which have $V-R < 1$. Furthermore, we use the D03 A_V curve, again scaled to match M06 at 8 kpc (§3.3). We take into account the detection completeness derived from the DOLPHOT simulations, which for the magnitude range chosen is $\sim 92\%$ on average. We find that about 3.8 times more stars are predicted than we observe in the R_{625} images ($\sim 10^5$ versus $2.6\ 10^4$). For an increase (decrease) of A_V by 50%, this factor is 3.1 (4.5).

For now we do not explore in detail the origin(s) of this discrepancy that could be due to the Galaxy model, differences between the local and bulge luminosity functions, or uncertainties in A_V. We simply reduce the number of expected CVs by this factor, which gives ~ 210–630 CVs expected for the A_V adopted (260–790 and 180–540 if A_V is 50% higher or lower).

We simulate our detection efficiency for CVs in a similar way as Koenig et al. (2008). We create a sample of 10^6 fake CVs to which we randomly assign an X-ray luminosity L_X and $f_X/f_R \approx f_X/f_V$ ratio based on the observed distributions by Verbunt et al. (1997), and a distance somewhere between us and d_{max}. We assume the CV-density profile follows the stellar-density profile by Picaud & Robin (2004) but scale it to match the local CV density. We make sure that the combination of distance, L_X and f_X/f_V does not give an absolute optical magnitude outside the observed range for CVs, $+3 \lesssim M_V \lesssim +12$ (Patterson 1998). For each fake CV we then assess whether it falls above the detection limit in the *Chandra* data (for a 10-keV thermal-bremsstrahlung model and a flux limit corresponding to 15 net counts (B_x) or $S/N_{B_x} \approx 3$) and in the ACS images (we use $R_{625,lim} = 24$, slightly fainter than LW 1 and LW 4; for fainter stars the detection completeness drops below $\sim 30\%$), after taking into account extinction. The resulting detection efficiency is about 17%. This number does not depend much on the choice of X-ray spectrum (a 2-keV thermal bremsstrahlung model gives a similar result), but is sensitive to A_V: an increase in A_V by 50% reduces the efficiency to 6%, while a 50% decrease gives an efficiency of 32%. The efficiency is further reduced by a factor 0.7–0.8 (depending on $B_{435}-R_{625}$ color) to $\sim 13\%$ (4.4% or 24% if A_V is 50% higher or lower) after taking into account the three-band detection completeness of the optical photometry. The simulated efficiency still overestimates the real efficiency. For example, a fraction of CVs have no or weak Hα emission lines (e.g. dwarf novae in outburst) and would consequently not be selected as candidate CVs.

In summary, the predicted number of CVs is at most $\sim 0.13\times 210=27$ to $\sim 0.13\times 630=80$ for the nominal A_V (12–35 or 43–130 if A_V is 50% higher or lower) where the lower and upper ends of the ranges are for a local CV density $1\ 10^{-5}$ and $3\ 10^{-5}$ pc^{-3}. This should be compared to three likely CVs and 21 possible CVs detected with net counts consistent with 15 (within 2σ) or more. At face value, this implies that the ratio of the CV and stellar densities in the bulge is similar to or lower than the local value. If this ratio is indeed between $6.9\ 10^{-5}$ and $2.1\ 10^{-5}$, it suggests a local CV density closer to $1\ 10^{-5}$ pc^{-3} (corresponding to the lower of the two ratios) than to $3\ 10^{-5}$pc^{-3}. In that case, at 8.2 kpc a peak in the CV density towards the LW is reached of $\sim 7\ 10^{-4}$ pc^{-3}; averaged over the bulge (7–10 kpc) the density would be $6.2\ 10^{-4}$ pc^{-3}. In the extreme case that none of our 21 possible CVs turn out to be true CVs, the relative CV density decreases towards the bulge, and/or we have severely overestimated our detection efficiency, and/or A_V is higher than our nominal value (which we know is the case in at least part of our field). Given the uncertainties (in the L_X and f_X/f_V distributions, A_V, X-ray and optical spectra) and the small sample, we cannot draw firm conclusions. In a follow-up paper where we report on the search for candidate CVs in the other two Windows, the constraints on the bulge CV density will be reconsidered with improved statistics.

5.3. *The hard X-ray sources in the central bulge*

One of our main goals is to investigate the nature of the hard (2–8 keV) source population in the central bulge that culminates in the high concentration of sources around SgrA*. H09 found that the dominating source classes in the SgrA* field and in the LW have similar X-ray properties, and could be part of a single bulge population whose projected number density is roughly inversely proportional to the angular offset from the Galactic Center. This implies that the suggestion by Muno et al. (2004), viz. that the majority of hard sources around SgrA* are magnetic CVs in the bulge (specifically: intermediate polars), should also hold true for the LW. We have identified two hard LW sources, LW 1 and LW 3, as plausible magnetic CVs. Below we investigate if all hard Galactic sources in the ACS mosaic ($\sim$10±4 in total, i.e. the number of sources with S/N_{H_c}>3 minus the contribution from AGN and the two coronal sources; §4.3) can be accounted for by bulge CVs.

For a spatial distribution that follows the normal star density and is subject to the selection effects described in §5.2, it is expected that about two-thirds of all observed CVs lie between 7–10 kpc. Let us assume that LW 1 and LW 3 indeed lie in the bulge. For convenience we put them at the Galactic-Center distance according to the Picaud & Robin (2004) model, i.e. at 8.5 kpc, which means their intrinsic absolute magnitudes are $M_{R_{625}} \approx 5.8$ and 4.3. They would represent only part of the total bulge CV population, since at 8.5 kpc only CVs with $M_{R_{625}} \lesssim +6$ can be detected (for $R_{625,lim}$=24). Based on the time-averaged M_V distribution of CVs by Patterson (1998), the fraction of CVs with $M_V \lesssim +6$ is $\sim$27% (for $V - R_{625} = 0$) or $\sim$41% (for $V - R_{625} = 1$). Other references give lower fractions. From our compilation of 31 CVs and CV candidates in globular and open clusters (47 Tuc, NGC 6397, M 67, NGC 6791) we find $\sim$16% and $\sim$29% for the two choices of $V - R_{625}$ color, respectively. Out of 24 nearby CVs with astrometric parallaxes (Thorstensen 2003; Thorstensen et al. 2008; Patterson et al. 2008) 1 (4%) has $M_V \lesssim +6$ while 3 (12%) have $M_V \lesssim +7$, where we have assumed $A_V = 0$ and have taken the observed V magnitude from Ritter & Kolb (2003). While clearly the M_V distribution is uncertain, these fractions are consistent with having optically identified only 2 out of 10±4 (14–33%) candidate bulge CVs, and therefore allow all hard, non-coronal sources in the ACS mosaic to be accounted for by bulge CVs (we assume that for CVs L_X and M_V are not correlated). This would imply an *observed* hard-CV density in the bulge of 0.74–$1.7 \, 10^{-5}$ pc^{-3}, assuming these sources lie between 7 and 10 kpc. To make this number match with the estimated total CV density in the bulge of $6.2 \, 10^{-4}$ pc^{-3} (§5.2), hard CVs must constitute between 1–3% of all bulge CVs. Despite uncertainties in the L_X and X-ray–spectral distributions of CVs, we make a rough estimate of how realistic this fraction is. Our hard sources have $L_X \gtrsim 4.2 \, 10^{31}$ ergs s^{-1} (2–8 keV) or $L_X \gtrsim 1.3 \, 10^{31}$ ergs s^{-1} (0.5–2 keV) for the X-ray spectra assumed. Comparing this to the ROSAT CVs in Verbunt et al. (1997) (0.5–2.5 keV), we estimate that we have observed the brightest $\sim$30% of CVs; therefore 4–9% of all CVs should be hard. To put this number in context: $\sim$13% and $\sim$10% of the CVs in the compilation by Ritter & Kolb (2003) are polars and intermediate polars, respectively, which typically have the hardest X-ray spectra among the known classes. On the other hand, Liebert et al. (2003) suggest a lower fraction of magnetic CVs, about $\sim$10%. In summary, according to our rough estimate, magnetic bulge CVs or IPs specifically offer a viable explanation for the hard Galactic sources in the LW if the CV-to-star ratio is constant.

LW 1 and LW 3 could be the first members of the inner-bulge hard-source population to be optically identified. If most hard sources near SgrA* indeed have the same nature as LW 1 and LW 3, there is no chance of finding their optical or infrared counterparts due to the much higher extinction towards the Galactic Center. We note that not one of the hard LW sources matches with a bright ($R_{625} < 17$) optical source, which implies that in the LW they are not dominated by wind-fed Be HMXBs. Their bright companions cannot be missed: a typical B0V secondary with $M_V = -4$ and $V - R \approx -0.1$, seen through $A_V = 4.2$, would have $R_{625} \approx 14.7$ at 8.5 kpc and $R_{625} \approx 16.3$ at twice that distance. The same conclusion was reached for the hard sources around SgrA* (Laycock et al. 2005).

6. CONCLUSIONS

We have searched for CVs in a low-extinction bulge field at a 1.4° angular separation from the Galactic Center. We discovered three likely CVs and 22 additional candidates that could also be coronally-active stars or background galaxies. Distance estimates place these systems at $\gtrsim$2 kpc. We investigate the CVs space density towards the bulge and find no large discrepancy between the number of observed and expected CVs in the direction of our field if the CV-to-star ratio is fixed at the local value. In that case, a local CV density of $1 \, 10^{-5}$ pc^{-3} is preferred by our findings. However, low statistics and uncertainties in the extinction and X-ray and optical properties of CVs prevent us from drawing firm conclusions. We will address the issue of the bulge CV density in more detail in similar studies of other low-extinction fields.

We identify two hard X-ray sources as plausible CVs. Their X-ray properties are similar to those of the bulk of the *Chandra* sources around SgrA*. If the Galactic-Center hard (2–8 keV) X-ray source population extends out to the field studied in this paper, as suggested by H09, these two systems could be the first optically identified members of this elusive population. We suggest that the other hard Galactic sources in our field can also be explained by CVs. This makes the sources presented in this paper prime targets for further study. Ground-based optical spectroscopy will be impossible for candidates like LW 1, but we encourage follow-up work on the more isolated ones. With the $\sim$900 ks *Chandra* exposure of our field described in Revnivtsev et al. (2009), the X-ray spectral and variability properties of the sources can be studied in more detail allowing one to place better constraints on their nature.

Facilities: CXO (ACIS), HST (ACS/WFC)

REFERENCES

Ak, T., Bilir, S., Ak, S., & Eker, Z. 2008, New Astronomy, 13, 133
Bahcall, J. N., & Soneira, R. M. 1980, ApJS, 44, 73
Bassa, C. G., Pooley, D., Verbunt, F., Homer, L., Anderson, S. F., & Lewin, W. H. G. 2008, A&A, 488, 921
Bessell, M. S. 1991, AJ, 101, 662
Carroll, B. W., & Ostlie, D. A. 1996, An Introduction to Modern Astrophysics (Institute for Mathematics and Its Applications)
Dempsey, R. C., Linsky, J. L., Fleming, T. A., & Schmitt, J. H. M. M. 1993, ApJSS, 86, 599
Dempsey, R. C., Linsky, J. L., Fleming, T. A., & Schmitt, J. H. M. M. 1997, ApJ, 478, 358
Dolphin, A. E. 2000, PASP, 112, 1383
Drimmel, R., Cabrera-Lavers, A., & López-Corredoira, M. 2003, A&A, 409, 205
Grindlay, J. et al. 2005, ApJ, 635, 920
Güdel, M. 2004, A&A Rev., 12, 71
Heinke, C. O., Ruiter, A. J., Muno, M. P., & Belczynski, K. 2008, in American Institute of Physics Conference Series, Vol. 1010, A Population Explosion: The Nature & Evolution of X-ray Binaries in Diverse Environments, ed. R. M. Bandyopadhyay, S. Wachter, D. Gelino, & C. R. Gelino, 136–142
Hong, J., Schlegel, E. M., & Grindlay, J. E. 2004, ApJ, 614, 508
Hong, J., van den Berg, M., Grindlay, J., Laycock, S., & Zhao, P. 2009, ApJ (submitted); http://hea-www.harvard.edu/ChaMPlane/papers.html
Hong, J., van den Berg, M., Schlegel, E., Grindlay, J., Koenig, X., Laycock, S., & Zhao, P. 2005, ApJ, 635, 907
Jacoby, G. H., Hunter, D. A., & Christian, C. A. 1984, ApJS, 56, 257
Kim, M., Wilkes, B. J., Kim, D.-W., Green, P. J., Barkhouse, W. A., Lee, M. G., Silverman, J. D., & Tananbaum, H. D. 2007, ApJ, 659, 29
Koekemoer, A., McLean, B., McMaster, M., & Jenkner, H. 2005, Instrument Science Report ACS 2005-06, Tech. rep., STScI
Koenig, X., Grindlay, J. E., van den Berg, M., Laycock, S., Zhao, P., Hong, J., & Schlegel, E. M. 2008, ApJ, 685, 463
Krautter, J. et al. 1999, A&A, 350, 743
Laycock, S., Grindlay, J., van den Berg, M., Zhao, P., Hong, J., Koenig, X., Schlegel, E. M., & Persson, S. E. 2005, ApJL, 634, L53
Liebert, J., Bergeron, P., & Holberg, J. B. 2003, AJ, 125, 348

Marshall, D. J., Robin, A. C., Reylé, C., Schultheis, M., & Picaud, S. 2006, A&A, 453, 635
Mochnacki, S. W. et al. 2002, AJ, 124, 2868
Muno, M. P. et al. 2004, ApJ, 613, 1179
—. 2003, ApJ, 589, 225
Patterson, J. 1984, ApJS, 54, 443
—. 1998, PASP, 110, 1132
Patterson, J., Thorstensen, J. R., & Knigge, C. 2008, PASP, 120, 510
Pfahl, E., Rappaport, S., & Podsiadlowski, P. 2002, ApJL, 571, L37
Picaud, S., & Robin, A. C. 2004, A&A, 428, 891
Predehl, P., & Schmitt, J. H. M. M. 1995, A&A, 293, 889
Pretorius, M. L., Knigge, C., O'Donoghue, D., Henry, J. P., Gioia, I. M., & Mullis, C. R. 2007, MNRAS, 382, 1279
Revnivtsev, M., Sazonov, S., Churazov, E., Forman, W., Vikhlinin, A., & Sunyaev, R. 2009, Nature, 458, 1142
Ritter, H., & Kolb, U. 2003, A&A, 404, 301
Schmitt, J. H. M. M., & Liefke, C. 2004, A&A, 417, 651
Sirianni, M. et al. 2005, PASP, 117, 1049
Stanek, K. Z., Udalski, A., Szymanski, M., Kaluzny, J., Kubiak, M., Mateo, M., & Krzeminski, W. 1997, ApJ, 477, 163
Stocke, J. T., Morris, S. L., Gioia, I. M., Maccacaro, T., Schild, R., Wolter, A., Fleming, T. A., & Henry, J. P. 1991, ApJS, 76, 813
Szkody, P. et al. 2002, AJ, 123, 430
Thorstensen, J. R. 2003, AJ, 126, 3017
Thorstensen, J. R., Lépine, S., & Shara, M. 2008, AJ, 136, 2107
van den Berg, M. et al. 2006, ApJL, 647, L135
Verbunt, F., Bunk, W. H., Ritter, H., & Pfeffermann, E. 1997, A&A, 327, 602
Warner, B. 1995, Cataclysmic variable stars (Cambridge Astrophysics Series, Cambridge, New York: Cambridge University Press, —c1995)
Wheatley, P. J., Verbunt, F., Belloni, T., Watson, M. G., Naylor, T., Ishida, M., Duck, S. R., & Pfeffermann, E. 1996, A&A, 307, 137
Zacharias, N., Urban, S. E., Zacharias, M. I., Wycoff, G. L., Hall, D. M., Monet, D. G., & Rafferty, T. J. 2004, AJ, 127, 3043
Zhao, P., Grindlay, J., Hong, J., Laycock, S., Koenig, X., Schlegel, E., & van den Berg, M. 2005, ApJS, 161, 429

TABLE 1
Chandra sources in the ACS field of view

CXOPS J	S/N_{H_c}	ID (table)
175139.2−293434	−0.51	…
175138.7−293519	2.83	…
175137.5−293602	0.42	LW 28 (5)
175137.4−293515	6.74	LW 41 (5)
175133.6−293313	6.38	LW 19 (4)
175133.3−293430	3.87	LW 42 (5)
175131.4−293446	1.42	…
175130.8−293736	6.07	…
175130.7−293232	5.18	LW 20 (4)
175130.0−293613	6.73	LW 17 (4)
175129.5−293602	1.52	LW 29 (5)
175129.4−293446	3.58	…
175128.1−293650	2.18	…
175127.8−293510	3.50	LW 43 (5)
175127.0−293706	4.24	LW 16 (4)
175124.1−293738	6.16	LW 3 (3)
175123.5−293755	4.19	LW 25 (4)
175122.4−293450	2.74	…
175121.7−293501	4.14	…
175120.9−293318	9.16	LW 1 (3)
175119.9−293458[a]	3.90	…
175119.9−293321	3.56	…
175119.1−293740	4.60	LW 15 (4)
175118.9−293733	1.31	LW 30 (5)
175142.8−293734	0.21	LW 13 (3)
175142.0−293401	3.03	…
175140.8−293736	3.31	…
175140.2−293318	1.66	…
175140.0−293557	1.70	LW 4 (3)
175139.7−293546	0.27	LW 31 (5)
175139.6−293811	3.42	LW 23 (4)
175138.5−293517	1.98	…
175138.2−293658	0.61	…
175137.2−293702	2.59	…
175136.4−293747	3.08	LW 32 (5)
175135.6−293754	2.63	LW 5 (3)
175135.3−293358	0.50	…
175135.1−293636	1.73	…
175134.8−293809	4.53	LW 11 (3)
175133.3−293620	0.45	…
175132.5−293636	3.64	LW 33 (5)
175132.2−293454	3.27	…
175130.6−293631	1.27	…
175130.6−293227	1.49	LW 26 (5)
175130.1−293212	0.12	…
175129.9−293206	5.11	…
175129.4−293331	0.86	…
175128.9−293412	2.11	LW 24 (4)
175128.5−293328	0.91	…
175127.9−293508	2.11	LW 14 (4)
175127.2−293243	2.63	…
175126.8−293228	2.06	…
175124.8−293830	2.57	…
175124.1−293756	1.15	…
175124.0−293532	1.10	LW 22 (4)
175122.8−293514	0.01	LW 6 (3)
175122.7−293436	3.52	…
175121.8−293820	4.31	…
175120.7−293417	2.67	LW 21 (4)
175120.5−293331	2.50	…
175120.3−293811	0.68	…
175119.6−293249	1.88	…
175119.1−293551	1.67	LW 34 (5)

TABLE 2
Chandra SOURCES IN THE ACS FIELD OF VIEW

CXOPS J	S/N_{H_c}	ID (table)
175119.1−293646	1.16	…
175118.7−293811	4.36	LW 8 (3)
175118.5−293732	2.86	LW 9 (3)
175118.4−293431	1.60	…
175118.1−293332	0.30	LW 2 (3)
175116.9−293716	0.73	…
175115.1−293355	2.31	…
175114.2−293224	2.89	LW 18 (4)
175113.8−293447	3.30	…
175113.6−293819	1.21	…
175113.5−293634	1.04	…
175111.8−293259	5.27	LW 7 (3)
175141.4−293508	2.05	LW 12 (3)
175139.8−293750	2.59	…
175137.3−293409	1.42	LW 35 (5)
175134.6−293609	1.62	…
175131.0−293216	1.72	LW 36 (5)
175123.7−293843	2.15	…
175123.2−293548	1.57	…
175119.3−293813	1.48	…
175114.5−293756	2.31	LW 37 (5)
175133.2−293718	0.70	LW 38 (5)
175137.6−293601	2.26	…
175134.5−293351	1.24	…
175133.8−293431	1.22	…
175128.6−293746	1.56	…
175119.3−293624	1.82	…
175115.8−293802	1.18	LW 10 (3)
175129.6−293331	1.56	…
175138.8−293409	1.23	LW 39 (5)
175138.3−293308	0.49	LW 40 (5)
175133.5−293515	−0.31	…
175120.9−293729	−0.02	…
175119.2−293801	0.55	…
175128.1−293703	−0.04	LW 27 (5)
175130.7−293825	0.98	…
175128.0−293815	−0.15	…

[a]The 95% error radius of this source lies partly in the chip gap.

For each *Chandra* source in the field of the ACS mosaic we list the source
name and signal-to-noise ratio in the hard band (H_c=2–8 keV). If appropriate,
we also give the short name adopted in this paper and (in parentheses) the
number of the table with the X-ray and optical properties. A negative value
of S/N_{H_c} indicates that the source was not significantly detected in the H_c
band.